Nature Communications

https://doi.org/10.1038/s41467-026-70579-w

Article in Press

Vacuum-induced interfacial compaction for scalable fabrication of high-performance organic solar cells

Received: 13 October 2025

Accepted: 2 March 2026

Cite this article as: Wang, S., Ding, R., Zhang, Z. *et al.* Vacuum-induced interfacial compaction for scalable fabrication of high-performance organic solar cells. *Nat Commun* (2026). https://doi.org/10.1038/s41467-026-70579-w

Siying Wang, Ruxue Ding, Ziyang Zhang, Yawei Liu, Jiarui Wang, Jiali Weng, Yao Zhao, Jianqi Zhang, Zihao Xu, Zheng Tang, Yunhao Cai & Hui Huang

Vacuum-induced Interfacial Compaction for Scalable Fabrication of High-performance Organic Solar Cells

Siying Wang[1#], Ruxue Ding[1#], Ziyang Zhang[1], Yawei Liu[2], Jiarui Wang[3], Jiali Weng[4], Yao Zhao[2], Jianqi Zhang[5], Zihao Xu[2], Zheng Tang[4], Yunhao Cai[1*] and Hui Huang[1,3*]

[1] College of Materials Science and Opto-Electronic Technology
University of Chinese Academy of Sciences
Beijing 100049, China

[2] Institute of Chemistry
University of Chinese Academy of Sciences
Beijing 100089, China

[3] School of Chemical Engineering and Technology, State Key Laboratory of Chemical Engineering and Low-Carbon Technology
Tianjin University
Tianjin 300072, China

[4] College of Materials Science and Engineering
Donghua University
Shanghai 201620, China

[5] Key Laboratory of Nanosystem and Hierarchical Fabrication
National Center for Nanoscience and Technology
Beijing 100190, China

[#] These authors contributed equally: Siying Wang, Ruxue Ding.

* Corresponding author email address: caiyunhao@ucas.ac.cn; huihuang@ucas.ac.cn.

ABSTRACT

Organic solar cells hold great promise for next-generation photovoltaics, yet their practical deployment is impeded by intrinsic morphological and interfacial limitations that compromise device performance and stability. Herein, we introduce a vacuum-induced interfacial compaction strategy that forms smooth, compact, and strongly adhered multilayer films without conventional thermal or solvent annealing, by promoting dense stacking, suppressing interfacial voids, and improving overall interfacial integrity. Consequently, corresponding devices achieve power conversion efficiencies of 20.51% for rigid and 19.13% for flexible devices, together with a high yield. Notably, device with an active area of 1.0 cm^2 and a module with an area of 15.7 cm^2 fabricated with this strategy deliver efficiencies of 19.04% and 17.48%, respectively. Upon further scaling the module area to 67.2 cm^2, a high efficiency of 15.37% is still attained. These results establish the vacuum-induced interfacial compaction strategy as a feasible route toward durable, high-performance organic solar cells.

INTRODUCTION

Organic solar cells (OSCs) have garnered considerable attention as a next-generation photovoltaic technology, owing to their inherent advantages, such as lightweight characteristics, mechanical flexibility, compatibility with roll-to-roll fabrication[1-3]. These features make OSCs particularly appealing for emerging applications in portable, wearable, and building-integrated electronics.

Over the past decade, great strides have been made in boosting power conversion efficiencies (PCEs), largely driven by innovations in material design, interfacial engineering, and device architecture innovation[4-6]. However, the translation of the high efficiencies from laboratory-scale devices to large-area and flexible modules with high yield and reproducibility remains chanllenging[7-10].

Morphological control and interfacial optimization are crucial for all OSCs, and these issues become more pronounced in flexible and large-area devices. The inherent softness of flexible substrates and the extended dimensions of larger area films exacerbate morphological and interfacial instabilities[11-15]. Even slight variations in film uniformity or interlayer contact can accumulate over extended areas, leading to local current mismatches, interfacial delamination, and severe performance fluctuations[16-19]. Conventional post-deposition treatments such as thermal or solvent annealing can mitigate some of these problems, yet they are typically incompatible with temperature-sensitive flexible substrates and continuous large-area fabrication[20-22]. Moreover, such treatments often induce uncontrolled solvent redistribution or interfacial stress accumulation, ultimately compromising mechanical integrity and reproducibility[23-27]. These observations emphasize the critical need for strategies that are capable of promoting film continuity, enhancing interlayer adhesion, and improving the performance across both rigid and flexible, small-area and large-area devices[28-31].

In this work, we develop a vacuum-induced interfacial compaction (VIC) strategy that fulfills these requirements by applying controlled vacuum pressure during key fabrication stages, without the need for conventional thermal or solvent treatments. This process promotes compact molecular

stacking, removes residual solvent, and enforces intimate interfacial contact, effectively eliminating voids and suppressing surface roughness variations across the entire substrate[32-33]. Distinct from conventional thermal annealing approach, VIC is compatible with low-temperature processing, making it particularly advantageous for flexible and larger area devices[34]. Systematic characterizations reveal that VIC not only strengthens interlayer adhesion and mitigates interfacial defect formation, but also yields smoother morphologies, reduces moisture ingress, and markedly improves mechanical robustness. Notably, the VIC strategy demonstrates broad applicability across diverse OSC systems, D18:L8-BO based devices deliver PCEs of 20.51% for small-area rigid devices (certified as 20.21%) and 19.13% for flexible OSCs, with good resistance to cyclic mechanical stress and high device yield. Moreover, this strategy is readily applicable to larger area devices. PCEs of 19.04% and 17.48% (certified as 17.04%) are achieved for 1.0 cm^2 and 15.7 cm^2 devices, respectively, representing the highest efficiency for binary 1.0 cm^2 and module OSCs with comparable active areas. Moreover, for 67.2 cm^2 module, a high efficiency of 15.37% is also obtained. These findings highlight the critical role of vacuum-assisted interface engineering as a scalable and substrate-independent strategy to address persistent challenges in advancing durable, high-performance organic photovoltaics.

RESULTS

VIC processing mechanism and optical properties

Fig. 1a schematically compares the VIC process with the conventional thermal annealing (TA) approach. In conventional TA process, thermal energy must sequentially pass through the substrate,

transparent conductive electrode, and transport layer before reaching the active layer. This indirect heating pathway often results in a spatially nonuniform temperature distribution across the active layer, which can adversely influence its morphology and interfacial contact quality, ultimately degrading device performance[35]. In contrast, the VIC treatment adopts a layer-by-layer consolidation strategy applied after the sequential deposition of the hole transport layer (2PACz) and the active layer. Rather than relying on thermal diffusion, VIC employs vacuum extraction at a pressure of approximately 1×10^{-4} bar to induce interfacial compaction under mild conditions. This process eliminates uncontrolled thermal effects, thereby preserving the intrinsic morphology of the active layer. Meanwhile, the applied vacuum assists in removing residual solvent and promotes intimate interfacial adhesion through negative-pressure-driven contact, leading to improved film uniformity and more efficient charge transport across interfaces.

D18:L8-BO was selected as the active layer to investigate the efficacy of the VIC strategy on the photovoltaic performance of OSCs. The chemical structures of D18[36] and L8-BO[37] are presented in Fig. 1b. UV-vis absorption measurements were carried out to evaluate the impact of different post-treatment methods on molecular aggregation behavior. Distinct absorption spectra behavior of the donor and the acceptor can be observed (Supplementary Fig. 1). The absorption spectra of D18 remained unchanged after TA and VIC treatments, maintaining identical absorption maxima and vibrionic features. In contrast, the absorption peak of L8-BO exhibited a red shift of 17 nm after VIC compared to TA treatment. This red shift indicates enhanced molecular ordering and stronger π-π stacking of L8-BO molecules induced by the VIC treatment. Meanwhile, the UV-vis absorption spectrum of the D18:L8-BO blend film exhibited the same trend (Fig. 1c).

The maximum absorption coefficients of TA and VIC treated films are 1.67×10^{-3} and 1.86×10^{-3} cm^{-1}, respectively (Supplementary Fig. 2). The enhanced absorption coefficient of the VIC-processed film contributes to the higher short-circuit current (J_{sc}) observed in the corresponding device. Furthermore, based on the absorption and emission spectra of L8-BO films (Supplementary Fig. 1), the Stokes shift (Δv) after TA and VIC treatments was calculated (Supplementary Table 1). The VIC-treated film exhibited a smaller Δv value (1413 cm^{-1}) compared to the TA-treated film (2076 cm^{-1}). This indicates that VIC treatment can enhance the rigidity of L8-BO molecules and reduce the reorganization energy[38].

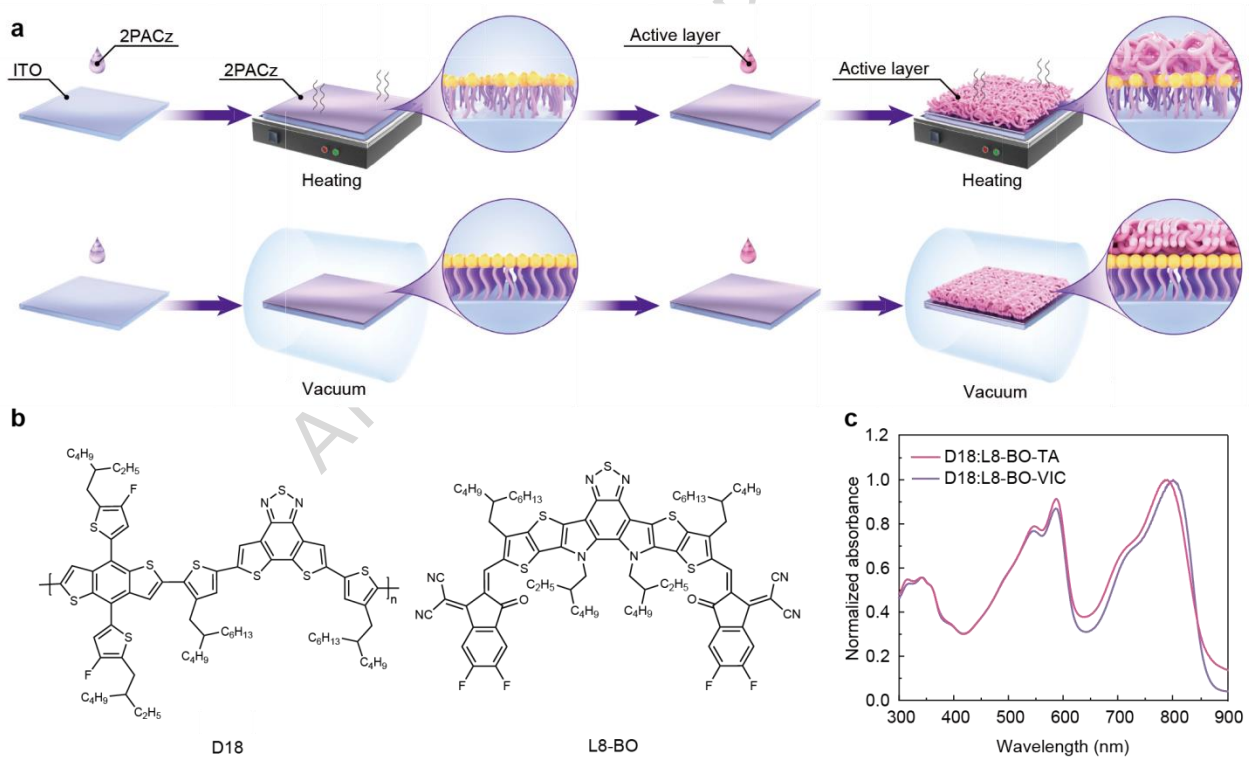

Fig. 1 | Schematic illustration, molecular structures, and optical properties. a Schematic diagram comparing the VIC with TA approach. **b** Chemical structures of polymer donor D18 and small-molecule acceptor L8-BO. **c** UV-vis absorption spectra of the D18:L8-BO blend films processed with TA and VIC treatments.

Photovoltaic performance and scalability

Subsequently, we fabricated a series of OSCs with a conventional architecture of ITO/2PACz/active layer/PNDIT-F3N/Ag. Detailed fabrication procedures are provided in the Methods. The current density-voltage (*J-V*) characteristics and the corresponding device parameters for both TA- and VIC-processed devices are presented in Fig. 2a and Table 1, respectively. Compared to the TA-processed device (19.23%), the VIC-processed OSC exhibited an obvious enhancement in PCE to 20.51% (certified as 20.21%; Supplementary Fig. 3), with improved open-circuit voltage (V_{oc}) (0.901 *vs.* 0.908 V), higher J_{sc} (26.88 *vs.* 27.82 mA cm^{-2}), and enhanced fill factor (FF) (79.4% *vs*. 81.2%). The external quantum efficiency (EQE) spectra are shown in Fig. 2b. The integrated J_{sc} values derived from EQE measurements are in good agreement with those obtained from *J-V* measurements. The optimization details are provided in the Supplementary Table 2-4. Supplementary Fig. 4 presents the statistical distribution of PCEs for the devices, demonstrating the reproducibility and reliability of the high efficiency. We also fabricated devices without the SAM layer. The results indicate that the VIC-treated devices exhibit a higher PCE than their TA-treated counterparts (Supplementary Table 5). This finding elucidates the contribution of removing water or residual solvent to the improvement of device performance.

The universal applicability of the VIC method was further verified in four different photovoltaic systems: D18:Y6 (VIC 19.01% *vs*. TA 18.29%), D18-Cl:N3 (VIC 19.41% *vs*. TA 18.57%), PM6:L8-BO (VIC 19.24% *vs*. TA 18.13%) and PM6:Y6 (VIC 19.19% *vs*. TA 18.25%) (Supplementary Fig. 5 and Supplementary Table 6). These consistent improvements across diverse material systems demonstrate the broad versatility and effectiveness of the VIC strategy in enhancing device performance. Additionally, we have conducted photostability tests under

maximum power point (MPP) tracking, and the results (Supplementary Fig. 6) show that VIC-treated rigid devices exhibited enhanced photostability, retaining 80% of their initial PCE (T_{80}) for 310 h compared with TA-treated devices (205 h). Such a result demonstrates that the VIC strategy can also help improve the photostability of the devices.

The improvement in device performance achieved through VIC strategy highlights its promise as a scalable and practical approach for larger area and industrial production. Therefore, we first upscaled the device area to 1.0 cm^2. The VIC-treated 1.0 cm^2 devices maintained a PCE of 19.04%, with a V_{oc} of 0.911 V, a J_{sc} of 28.13 mA cm^{-2}, and an FF of 74.3% (Fig. 2c, Table 1). In contrast, the device processed with conventional TA treatment showed a much lower PCE of 17.56%, with a V_{oc} of 0.901 V, a J_{sc} of 26.70 mA cm^{-2}, and an FF of 73.0%. The EQE spectra of 1.0 cm^2 devices are shown in Supplementary Fig. 7. Encouraged by these results, we further fabricated 15.7 cm^2 and 67.2 cm^2 OSC modules (detailed fabrication procedures are provided in the Methods). For 15.7 cm^2 OSC module, the TA-treated module achieved a PCE of 15.01%, with a V_{oc} of 6.87 V, a J_{sc} of 3.26 mA cm^{-2}, and an FF of 67.02% (Fig. 2d, Supplementary Table 7). Notably, the VIC-treated module delivered an efficiency of 17.48% (certified as 17.04%; Supplementary Fig. 8), with a V_{oc} of 6.96 V, a J_{sc} of 3.34 mA cm^{-2}, and an FF of 75.19%, representing a record-high value for binary OSC modules with comparable device area. Notably, the relative PCE loss when scaling to 15.7 cm^2 modules was lower for VIC-treated devices (14.77%) compared to TA-treated devices (21.94%), demonstrating the superior scalability and reproducibility of the VIC approach (Fig. 2e). For 67.2 cm^2 OSC modules, a high efficiency of 15.37% was obtianed, with a V_{oc} of 14.06 V, a J_{sc} of 1.54 mA cm^{-2}, and an FF of 71.12%

(Supplementary Fig. 9 and Supplementary Table 8).

Table 1 | Photovoltaic parameters of small-area and 1.0 cm^2 devices based on different treatments.

Active layer	V_{oc} (V)	J_{sc} (mA cm^{-2})	FF (%)	PCE[a] (%)
D18:L8-BO-TA (small-area)	0.901 (0.896±0.010)	26.88 (26.62±0.50)	79.4 (78.7±1.8)	19.23 (18.78±0.92)
D18:L8-BO-VIC (small-area)	0.908 (0.906±0.002)	27.82 (27.52±0.20)	81.2 (80.6±0.5)	20.51 (20.12±0.24)
D18:L8-BO-TA (1.0 cm^2)	0.901 (0.858±0.031)	26.70 (25.38±0.85)	73.0 (68.2±3.5)	17.56 (14.92±1.77)
D18:L8-BO-VIC (1.0 cm^2)	0.911 (0.893±0.017)	28.13 (27.43±0.64)	74.3 (72.1±2.0)	19.04 (17.69±1.17)

[a] The average parameters were calculated based on 20 independent cells.

Charge transport and recombination dynamics

To investigate the influence of VIC treatment on charge transport, space-charge-limited current (SCLC) measurements and electrochemical impedance spectroscopy (EIS) analyses were performed (Fig. 2f, Supplementary Fig. 10 and Supplementary Table 9). Compared to the TA treatment, the VIC treatment enhanced both hole (μ_h) and electron (μ_e) mobilities of the devices as a result of μ_h increasing from 2.37 × 10^{-4} to 3.28 × 10^{-4} cm^2 V^{-1} s^{-1} and μ_e increasing from 2.12 × 10^{-4} to 3.20 × 10^{-4} cm^2 V^{-1} s^{-1}. Importantly, the VIC-processed device showed a more balanced charge transport with a μ_h/μ_e ratio of 1.02, compared to 1.12 for the TA-processed device. The higher mobility and more balanced transport contribute to the enhanced J_{sc} and FF observed in the VIC-processed device. The trap density (n_t) was determined from the trap-filled limit voltage (V_{TFL}) using the equation of

$$V_{\mathrm{TFL}} = \frac{en_tL^2}{2\varepsilon\varepsilon_0} \quad (1)$$

where e is the elementary charge, L is the active layer thickness, ε is the dielectric constant, and ε_0 represents the vacuum dielectric constant. The VIC-treated device exhibited a reduced trap density (1.56×10^{16} cm^{-3}) compared to the TA-processed device (1.67×10^{16} cm^{-3}). The suppressed n_t could help reduce the non-radiative recombination loss in the VIC-processed device. Besides, EIS measurements (1 Hz-100 MHz, under dark conditions) revealed different charge transport characteristics between the TA- and the VIC-processed devices. Nyquist plots were analyzed using the equivalent circuit model[39]. The derived equivalent circuit parameters are summarized in Supplementary Table 10. Compared to the TA treatment, the VIC processing reduced series resistance (R_s=21.4 *vs*. 25.2 Ω) while increasing shunt resistance (R_{sh}= 68.2 *vs*. 47.5 kΩ), indicative of enhanced charge collection efficiency and suppressed leakage currents in the devices. The impedance results confirm that the VIC processing concurrently improves charge transport and inhibits non-radiative recombination loss. Collectively, these results show that the VIC treatment mitigates interfacial defects, optimizes charge transport balance, and enhances interfacial contact quality, which explains the high efficiency of the corresponding devices.

The photocurrent density (J_{ph}) versus effective voltage (V_{eff}) of the TA- and the VIC-processed devices was examined (Fig. 2g). J_{ph} is defined as $J_{ph} = J_L - J_D$, where J_L and J_D stand for the current densities under illuminated and in the dark, respectively. V_{eff} is calculated by $V_{eff} = V_0 - V_a$, where V_0 is the voltage at which the photocurrent becomes zero and V_a is the applied bias voltage. The VIC-treated device exhibited superior charge extraction, as evidenced by both higher saturation photocurrent (J_{sat}) and faster J_{ph} saturation compared to the TA-processed device. The exciton dissociation and charge collection probability of the devices are determined by the J_{ph}/J_{sat}

values under the short-circuit and maximum power output conditions, respectively. The VIC-processed devices achieved P_{diss} and P_{coll} values of 98.56% and 90.32%, respectively, surpassing those of the TA-processed devices (96.95% and 85.49%). These results demonstrate that the VIC treatment enhances charge collection, synergistically boosting device performance.

The transient absorption spectroscopy was further carried out to probe the charge generation dynamics of OSCs. Supplementary Fig. 11a-b displays the two-dimensional color maps of transient absorption spectra for the films, while Supplementary Fig. 11c-d presents the corresponding transient absorption spectra recorded at different time delays. When D18 was excited at 750 nm, distinct ground state bleaching signals were detected at 585 nm (donor). The experimental data were analyzed using a tri-exponential fitting model incorporating one growth component and two decay processes (Supplementary Fig. 11e-f and Supplementary Table 11). The growth time constant (τ_1) corresponds to the rate of hole transfer occurring between D18 and L8-BO, whereas the weighted-average decay time constant (τ_{rec}) represents the timescale of charge recombination processes[40]. Comparative analysis of the fitting parameters demonstrated that the VIC-processed film showed faster charge transfer (τ_1 = 0.25 ± 0.04 *vs.* 0.67 ± 0.37 ps) and slower recombination (τ_{rec} = 3.04 ± 0.56 *vs.* 2.14 ± 0.40 ns) compared to the TA-treated film, indicating enhanced charge separation efficiency in the VIC-processed device.

To elucidate the charge recombination dynamics, the dependence of V_{oc} and J_{sc} on illumination intensity (P_{light}) was measured. Fig. 2h reveals a logarithmic relationship between V_{oc} and P_{light}. When the slope of V_{oc} versus the natural logarithm of P_{light} is equal to kT/q (where k is Boltzmann's constant, T is temperature, and q is the elementary charge), bimolecular

recombination is the dominant recombination mechanism. When the main recombination mechanism is trap-assisted recombination, a higher dependence of the V_{oc} on the light intensity (>kT/q) can be obtained. It can be seen that the VIC-processed device exhibited a lower slope (1.130 kT/q) than the TA-processed device (1.289 kT/q), indicating the reduced trap-assisted charge recombination in the VIC-processed device, consistent with the lower defect density confirmed by SCLC measurements. The relationship between the J_{sc} and P_{light} can be expressed by $J_{sc} \propto (P_{light})^{\alpha}$, where α is an exponential factor that reflects the extent of bimolecular charge recombination (Fig. 2i). The extracted α values for the TA- and VIC-processed devices were 0.989 and 0.994, respectively, indicative of weaker bimolecular recombination in the VIC-processed device.

To gain a deeper insight into the influence of VIC treatment on device performance, the energy loss (E_{loss}) in OSCs was systematically analyzed. Supplementary Fig. 12 shows the EQE and electroluminescence (EL) spectra of the devices fabricated with TA and VIC methods. The detailed energy loss values are summarized in Supplementary Table 12. Generally, the total E_{loss}, defined as

$$E_{loss} = E_g - qV_{oc} \quad (2)$$

can be divided into three parts. The inevitable radiative loss (ΔE_1) was determined by the Shockley-Queisser limit, yielding an identical theoretical open-circuit voltage (V_{oc}^{SQ} = 1.175 V) for both TA- and VIC-treated devices. The additional radiative recombination-related loss (ΔE_2) was derived from the dark saturation current density (J_0^{rad}) and the radiative recombination limit for the V_{oc} (V_{oc}^{rad}). The VIC-treated devices exhibited a marginally higher V_{oc}^{rad} value and

consequently a slightly lower ΔE_2 than the TA-treated devices, suggesting that the different treatments have a negligible effect on radiative recombination loss. In contrast, the non-radiative energy loss (ΔE_3) showed a more pronounced distinction. ΔE_3 can be calculated according to the equation of $\Delta E_3 = qV_{oc}^{rad} - qV_{oc}$. The ΔE_3 was reduced in the VIC-treated device (0.209 eV) compared to the TA-treated one (0.221 eV). Overall, the total energy losses for the VIC- and TA-treated devices were 0.527 and 0.540 eV, respectively. The aforementioned results indicate that VIC processing effectively mitigates defect formation and reduces non-radiative energy losses in the corresponding devices.

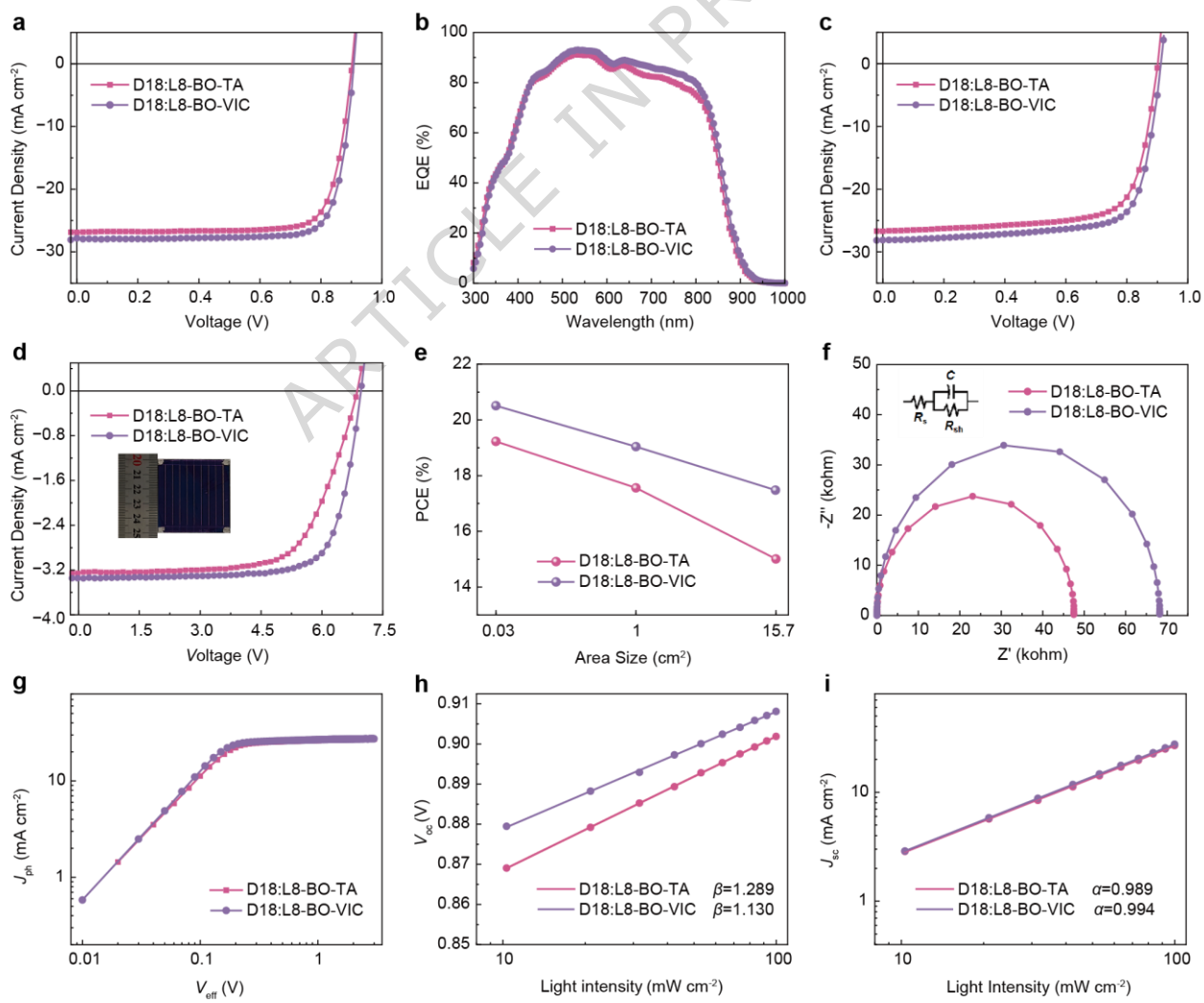

Fig. 2 | Photovoltaic performance and charge dynamics of OSCs. a *J-V* curves of the rigid small-area OSCs under AM 1.5G illumination. **b** EQE spectra of the corresponding devices. **c** *J-V* curves of the 1.0 cm^2 devices. **d** *J-V* curves of the 15.7 cm^2 modules. **e** The curve of PCE versus device area for TA- and VIC-processed devices. **f** Nyquist plots from electrochemical impedance spectroscopy measurements. **g** J_{ph} versus V_{eff} curves. **h** V_{oc} versus light intensity curves. **i** J_{sc} versus light intensity curves.

Morphology characterization

Atomic force microscopy (AFM) was employed to characterize the surface morphology of different processing conditions. Compared to the TA treatment, it was revealed that the VIC-processed 2PACz/AL film exhibited smoother interface, with a lower root-mean-square roughness (R_q) of 1.10 nm, compared to 1.47 nm for the TA-treated film (Fig. 3a-b). The reduction in surface roughness reflects the VIC process's ability to promote homogeneous film formation, thereby improving morphological stability and interfacial integrity[41]. We also performed Kelvin probe force microscopy (KPFM) to evaluate the nanoscale uniformity of the 2PACz films under different treatments. The analysis of the contact potential difference (CPD) distribution provides a metric for the uniformity of the molecular assembly (Supplementary Fig. 13). Our KPFM results reveal a narrower and more homogeneous CPD distribution for the VIC-treated 2PACz film, with a full width at half maximum (FWHM) of 24 mV. In contrast, the TA-treated film exhibits a broader distribution (FWHM = 31 mV), indicating increased nanoscale variability. These results suggest that even on small-area substrates the VIC treatment could promote a more uniform molecular assembly. The improved uniformity is expected to facilitate more efficient carrier extraction and reduced interfacial recombination.

Grazing incidence wide-angle X-ray scattering (GIWAXS) measurements were conducted to investigate the molecular packing and orientation of different films (Fig. 3c-d and Supplementary

Fig. 14a-b). The corresponding in-plane (IP) and out-of-plane (OOP) line-cut profiles are presented in Fig. 3e and Supplementary Fig. 14c. For 2PACz film, the crystal coherence length (CCL) values calculated from the π-π stacking peaks in the OOP direction increased from 96.62 Å (TA) to 123.14 Å (VIC) (Supplementary Table 13), confirming the enhanced crystallinity of the 2PACz by using the VIC treatment. Meanwhile, the VIC processing enhanced CCL of the active layer for both π-π stacking (18.15 *vs.* 17.02 Å) and lamellar stacking (79.49 *vs.* 69.01 Å) compared to the TA-treated film (Supplementary Table 14-15). These results collectively demonstrate that the VIC treatment promotes tighter molecular packing and enhanced crystallinity in both the 2PACz and active layers, which is beneficial for efficient charge transport within the devices.

Interfacial contact also plays an important role in determining the performance of OSCs. To evaluate the impact of VIC treatment, we examined wettability changes by measuring contact angles (θ) of deionized water and ethylene glycol on TA- and VIC-processed films (Supplementary Fig. 15). Notably, the hydrophobicity of both the interface layer (TA 49.12° *vs*. VIC 60.08°) and active layers (TA 89.45° *vs*. VIC 101.55°) was significantly enhanced after the VIC treatment, which can be attributed to the effective removal of volatile components and impurities under vacuum conditions. This enhanced hydrophobicity can suppress moisture ingress and improve device stability. Furthermore, surface tension (γ) analysis using Wu's model[42] and the derived Flory-Huggins interaction parameters (χ) revealed lower χ values for VIC-processed interfaces compared to TA-processed counterparts (2PACz/D18:L8-BO: 2.238 *vs.* 5.636; D18:L8-BO/PNDIT-F3N: 0.992 *vs.* 1.049), confirming improved interfacial compatibility and stronger molecular interactions (Supplementary Table 16).

To gain an insight into the interfacial interaction and potential adhesion enhancement, time-of-flight secondary ion mass spectrometry (TOF-SIMS) depth profiling on different films were conducted (Fig. 4a-b). Characteristic fragment ions including PO^{3-} for 2PACz, F^- for AL, and CNO^- for PNDIT-F3N layer served as effective molecular markers for interfacial analysis. The normalized depth profiles revealed that the VIC-treated films exhibited broader interfacial regions than their TA-treated counterparts, indicative of enhanced molecular interdiffusion and stronger interfacial coupling, which are key factors contributing to the improved adhesion.

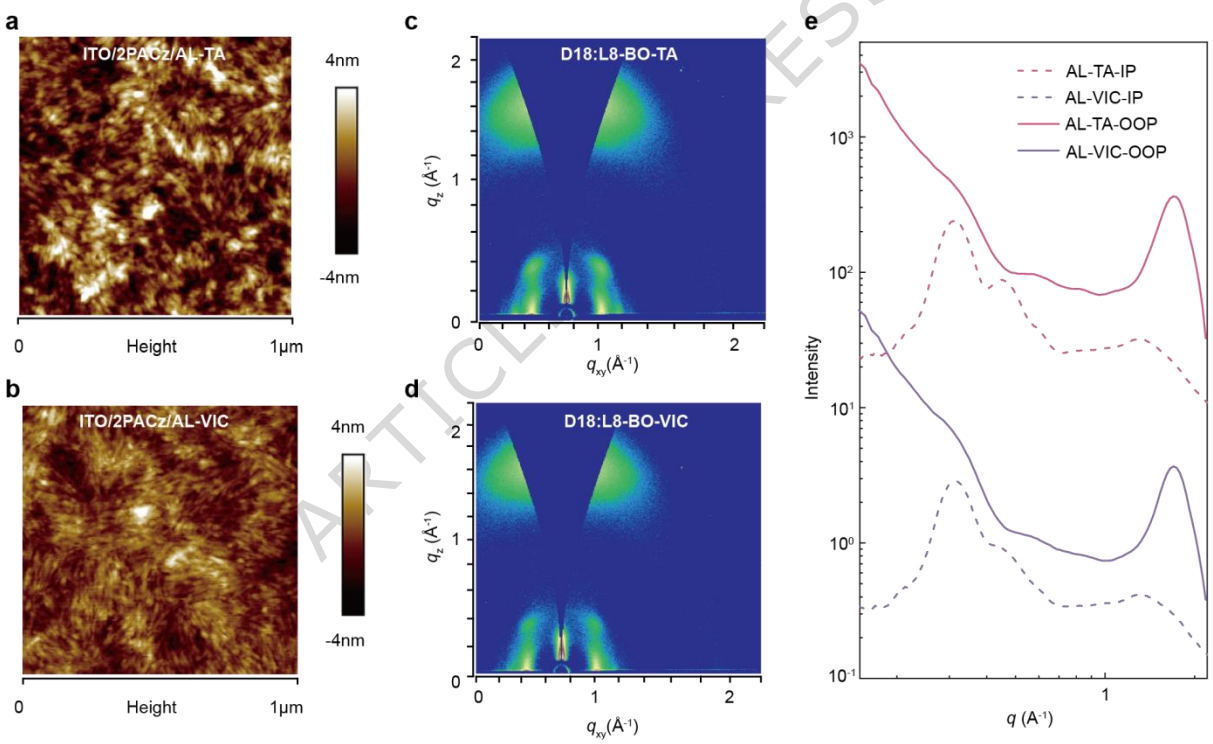

Fig. 3 | Morphology and molecular packing characterization. AFM height images (1 × 1 μm^2) of the 2PACz/active layer films processed with TA **(a)** and VIC **(b)**. 2D GIWAXS patterns of the D18:L8-BO blend films processed with TA **(c)** and VIC **(d)**. **e** Corresponding IP (dashed line) and OOP (solid line) 1D line-cut profiles from the GIWAXS data.

Flexible device performance

The above characterization reveals that the VIC treatment could enhance the interfacial

contact in processed films. Motivated by this improvement, we applied the VIC strategy to the fabrication of flexible OSCs to address interfacial delamination issues and improve device stability during mechanical deformation. A series of flexible OSCs with device architecture of Ag alloy/2PACz/active layer/PNDIT-F3N/Ag were fabricated. Fig. 4c shows the *J*-*V* curves of the optimal devices under the illumination of AM 1.5G, 100 mW cm^{-2}. Table 2 lists the detailed photovoltaic parameters of the flexible devices. Remarkably, the VIC-treated device achieved a PCE of 19.13%, along with a V_{oc} of 0.905 V, a J_{sc} of 26.29 mA cm^{-2}, and an FF of 80.4%, which is higher than the 17.70% efficiency of the TA-processed flexible device. The corresponding EQE spectra are shown in Supplementary Fig. 16. Moreover, device yield serves as a crucial indicator of the practical manufacturability of OSCs. Devices exhibiting PCE values below 80% of the maximum are categorized as defective. As summarized in Fig. 4d, yield statistics were compiled for 100 devices each of rigid small-area, flexible small-area, and rigid 1.0 cm^2 devices subjected to TA and VIC processing. The VIC-treated devices consistently exhibited higher yields (83% *vs.* 100% for rigid small-area, 77% *vs.* 100% for flexible, and 52% *vs.* 83% for rigid 1.0 cm^2 devices), indicating the robustness and scalability of the VIC strategy for practical production.

Photostability tests under MPP tracking revealed that VIC-treated flexible devices maintained T_{80} for 210 h, a 48.1% improvement over TA-treated counterparts (109 h) (Fig. 4e). Under accelerated thermal aging at 85 °C in nitrogen, VIC-processed devices retained 90.1% of their initial PCE after 60 h, compared with 86.0% for TA-treated devices (Supplementary Fig. 17). Mechanical bending tests (r = 5 mm) further confirmed superior durability, with VIC-treated devices maintaining 91.3% of their initial efficiency after 2000 cycles versus 83.2% for TA-treated

ones (Fig. 4f). Ambient stability testing (25 °C, 40-60% RH) showed that VIC-treated encapsulated devices preserved 80.0% of their initial PCE after 100 h, whereas TA-treated counterparts retained only 73.1% (Supplementary Fig. 18). These results demonstrate that the VIC strategy provides a useful approach to enhance the efficiency, mechanical robustness, and operational stability of flexible OSCs.

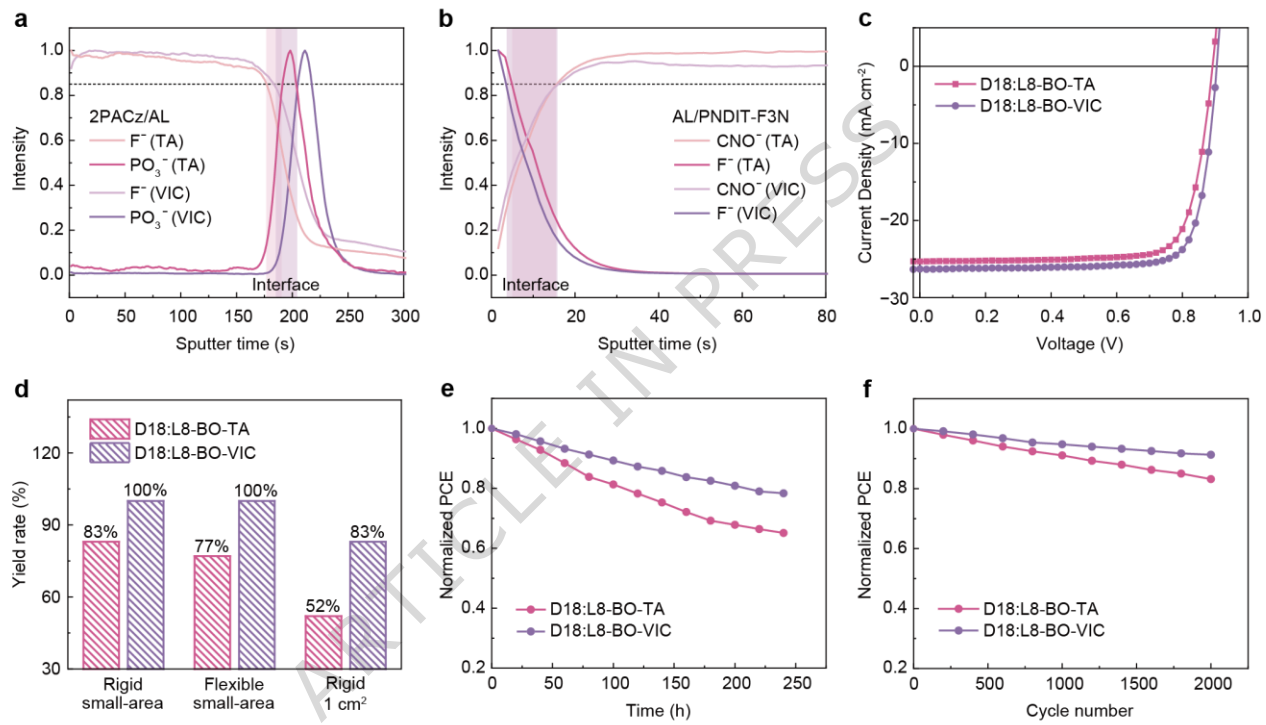

Fig. 4 | Interfacial adhesion, flexible device performance, and stability. TOF-SIMS depth profiles of the multilayer films processed with TA **(a)** and VIC **(b)**. **c** *J-V* curves of the flexible OSCs under AM 1.5G illumination. **d** Statistical yield rates of rigid small-area, flexible small-area, and rigid 1.0 cm^2 devices. **e** Normalized PCE of the flexible OSCs under maximum power point tracking over time. **f** Normalized PCE retention of the flexible OSCs as a function of bending cycles (bending radius = 5 mm).

Table 2 | Photovoltaic parameters of flexible D18:L8-BO devices based on different treatments.

Active layer	V_{oc} (V)	J_{sc} (mA cm^{-2})	FF (%)	PCE[a] (%)
D18:L8-BO-TA	0.891 (0.881±0.011)	25.31 (24.91±0.40)	78.5 (76.2±2.3)	17.70 (16.73±0.93)
D18:L8-BO-VIC	0.905 (0.902±0.002)	26.29 (26.05±0.19)	80.4 (79.8±0.4)	19.13 (18.75±0.17)

[a] The average parameters were calculated based on 20 independent cells.

To illustrate the interfacial contact property, we conducted 3M tape peeling and nano-scratch tests to measure adhesion strength at the ITO/2PACz, 2PACz/active layer and active layer/PNDIT-F3N interfaces. Corresponding results of peeling tests showed that the VIC-treated 2PACz/active layer and active layer/PNDIT-F3N samples maintained superior film integrity and higher peel strength than the TA-treated counterparts (Fig. 5a-d, Supplementary Fig. 19-20 and Supplementary Table 17). Then, we performed scanning electron microscopy (SEM) combined with energy dispersive X-ray spectroscopy (EDS) (Supplementary Fig. 21-24). Quantitative EDS mappings demonstrate pronounced atomic concentration gradients across interfaces, with characteristic element ratios summarized in Supplementary Table 18-20. The VIC-treated samples exhibited lower characteristic element ratios than the TA-treated samples (In/P: 0.34 *vs*. 0.65 for ITO/2PACz; P/F: 0.21 *vs*. 0.29 for 2PACz/active layer; F/C: 0.38 *vs*. 0.57 for active layer/PNDIT-F3N). These findings indicate that VIC processing more effectively preserves film uniformity and compositional integrity across multilayer interfaces.

Meanwhile, the adhesion strengths between different layers of ITO/2PACz/active layer samples were evaluated by nano-scratch tests (Fig. 5e-f). For nano-scratch tests, the critical loads identify at abrupt transitions in the curve marking interlayer failure points. The ITO/2PACz/active layer system exhibited a three-stage failure mechanism: Stage I involves active layer film deformation; Stage II shows 2PACz film response with smaller normal displacement under identical loading rates, indicating higher elastic modulus and hardness than active layer; Stage III represents complete 2PACz/AL rupture with direct probe-ITO contact and subsequent substrate scratching. The critical normal and lateral forces for active layer failure (NF_1, LF_1) and for 2PACz

failure (NF_2, LF_2) were extracted (Supplementary Table 21). The VIC-treated samples exhibited enhanced mechanical properties. For the active layer, the critical forces increased from NF_1 = 133 μN and LF_1 = 36 μN (TA-treated) to NF_1 = 213 μN and LF_1 = 70 μN (VIC-treated). Similarly, for the 2PACz layer, NF_2 and LF_2 values rose from 733 and 198 μN (TA-treated) to 750 and 208 μN (VIC-treated), respectively. This mechanical reinforcement is attributed to the negative pressure environment introduced by the VIC processing, which enhances interfacial adhesion. Stronger interfacial bonding not only suppresses delamination but also facilitates stress transfer and dissipation across layers, thereby mitigating crack initiation and propagation.

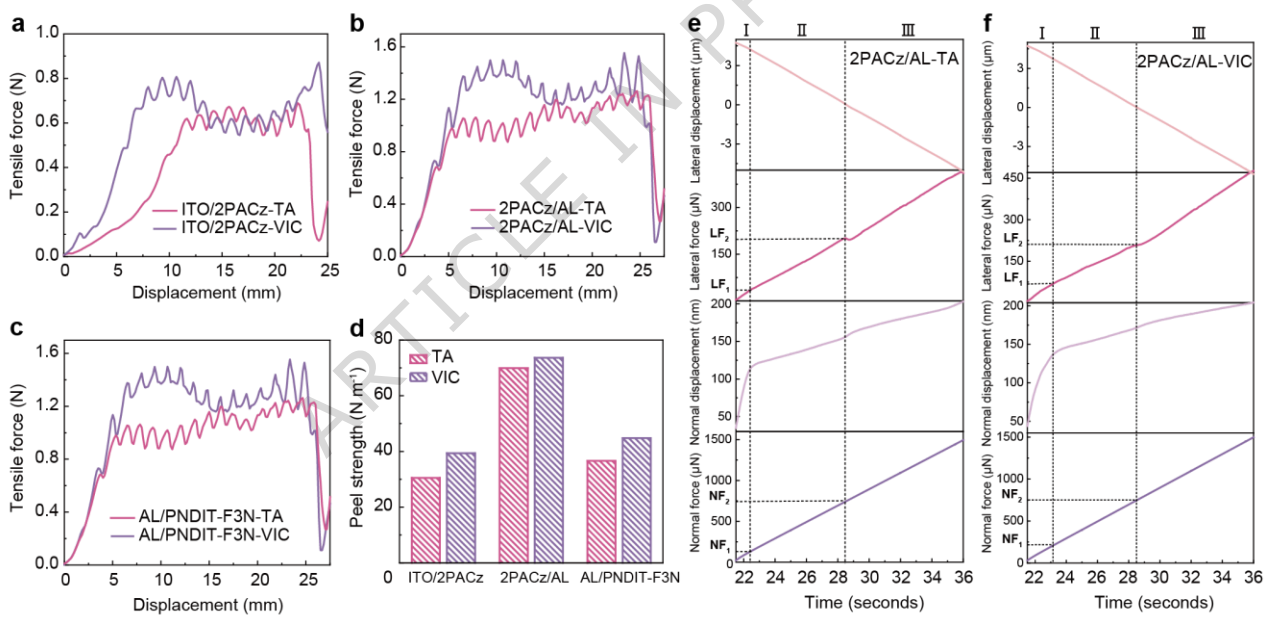

Fig. 5 | Quantitative assessment of interfacial mechanical adhesion. Tensile force-displacement curves obtained from peeling tests for the ITO/2PACz **(a)**, 2PACz/active layer **(b)**, and active layer/PNDIT-F3N **(c)** interfaces. **d** Calculated peel strength for the different interfaces and processing methods. Nano-scratch curves for the ITO/2PACz/active layer samples processed with TA **(e)** and VIC **(f)**.

To assess the influence of VIC treatment on interfacial contact and mechanical robustness of OSCs, we conducted nanoindentation and peak force quantitative nanomechanical mapping (PFQNM) analyses. SEM images after indentation (Fig. 6a-b) and force-displacement curves (Fig.

6c) revealed that VIC-treated films exhibited lower reduced modulus (E_r) values than their TA-treated counterparts (Supplementary Table 22). Notably, both 2PACz-VIC and AL-VIC films showed shallower residual indentation depths (h_f) (14.6 and 39.9 nm, respectively) than those of TA-treated films (16.2 and 45.8 nm), indicating enhanced resistance to plastic deformation. SEM imaging confirmed these results, showing smaller indentation areas for VIC-treated films and no visible cracks near stress-concentrated regions. Quantitative PFQNM analysis (Fig. 6d-i, Supplementary Fig. 25) based on Derjaguin-Muller-Toporov (DMT) theory further verified these trends. The VIC-treated 2PACz and active layer films showed a noticeable mechanical softening, with the DMT modulus decreasing from 1771 to 1625 MPa and from 1168 to 1042 MPa, respectively, compared to TA-treated counterparts. Correspondingly, their stiffness values dropped from 85.3 to 83.8 N m^{-1} and from 63.3 to 58.1 N m^{-1}, while the adhesion forces increased from 31.2 to 43.7 nN and from 32.9 to 44.6 nN, indicating improved interfacial compliance and stronger interlayer bonding. PFQNM images displayed expanded bright regions, indicative of more uniform and stronger interfacial adhesion. These combined enhanced adhesion and moderate softening suggest that VIC treatment facilitates stress dissipation during deformation while reinforcing interfacial bonding and suppressing delamination. Consequently, VIC-treated OSCs exhibit superior bending resistance and mechanical durability.

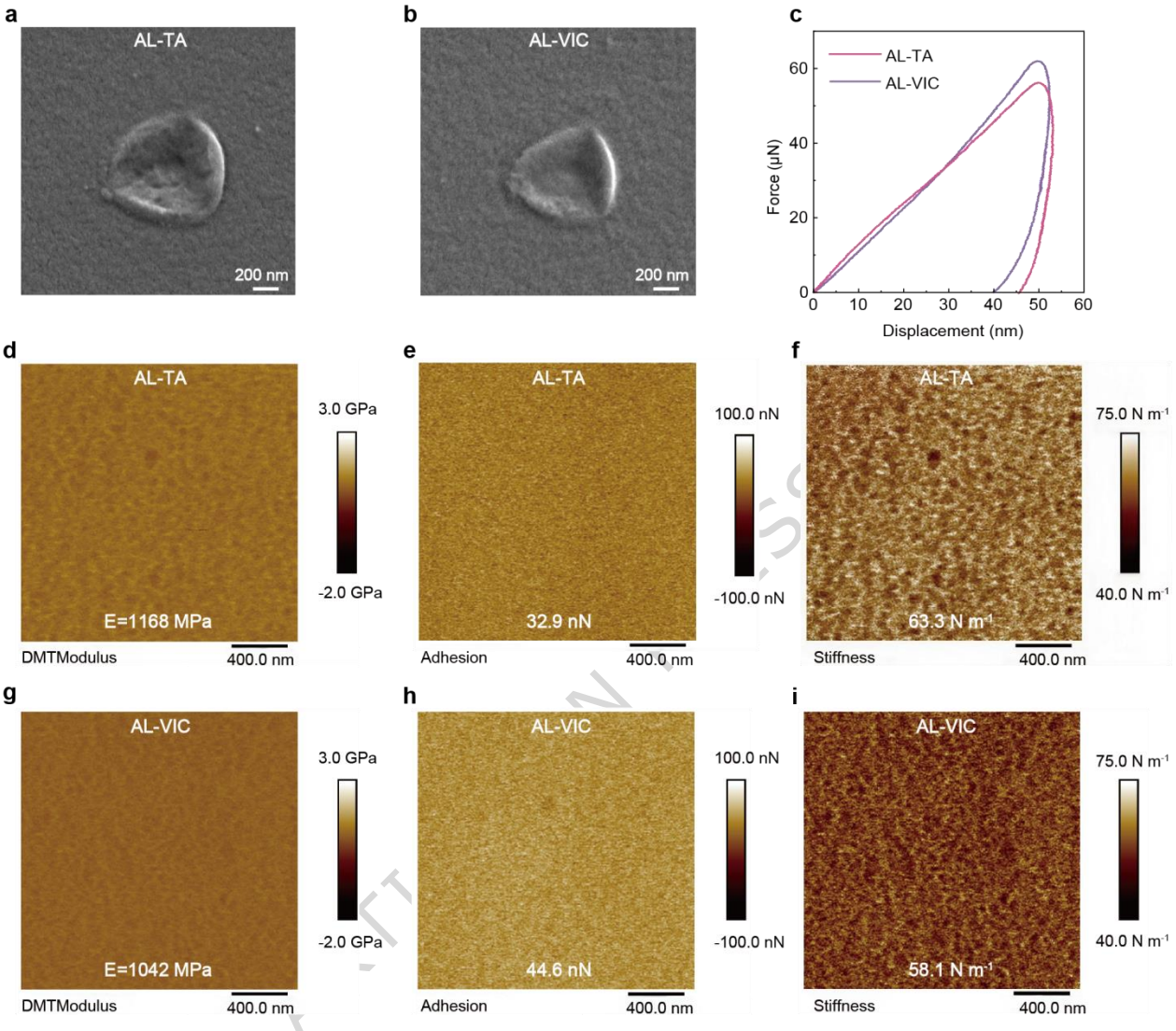

Fig. 6 | Nanomechanical properties of the functional layers. SEM images of the residual indentation on the 2PACz **(a)** and active layer **(b)** films after nanoindentation tests. **c** Representative force-displacement curves obtained from the nanoindentation tests. PFQNM images of the TA-processed active layer film: DMT modulus **(d)**, adhesion force **(e)**, and stiffness **(f)**. PFQNM images of the VIC-processed active layer film: DMT modulus **(g)**, adhesion force **(h)**, and stiffness **(i)**.

DISCUSSION

In summary, we have developed a VIC strategy that addresses critical morphological and mechanical challenges in OSCs. VIC promotes dense molecular packing and robust interfacial adhesion, making it particularly suitable for flexible and large-area device fabrication. Systematic

characterizations reveal that VIC-processed devices exhibit enhanced interlayer cohesion, reduced interfacial defects, optimized film morphology, and better photostability and mechanical stability. Upon using this strategy, PCEs of 20.51% in rigid D18:L8-BO-based OSCs, 19.13% for flexible binary devices, 19.04% for 1.0 cm^2 devices, 17.48% for 15.7 cm^2 module, and 15.37% for 67.2 cm^2 module. Besides, this strategy has been successfully validated across multiple photovoltaic systems. The combination of high efficiency, better yield, robust mechanical performance, and manufacturing compatibility position VIC as a promising solution for scalable production of high-performance organic photovoltaics.

METHODS

Materials

All reagents were purchased from the following suppliers and used as received unless otherwise specified: Inno-chem, J&K, 3A Chemicals, Derthon, Energy Chemical, Meryer Chemical Technology Co., Ltd., Beijing Mairuida Technology Co., Ltd., Sigma-Aldrich, and Alfa Aesar. D18 and L8-BO were obtained from Solarmer Materials Inc. 2PACz was sourced from Tokyo Chemical Industry Co., Ltd. Ag was acquired from ZhongNuo Advanced Material (Beijing) Technology Co., Ltd.

Device fabrication

The rigid devices were constructed with the following layer structure: ITO/2PACz/active layer/PNDIT-F3N/Ag. The geometrical design of small-area devices is shown in Supplementary

Fig. 26. Initially, ITO-coated glass substrates underwent sequential ultrasonic cleaning using detergent, deionized water, acetone, and anhydrous ethanol (20 min per solvent). Thereafter, the substrates were nitrogen-blown dried. Subsequently, the substrates were subjected to UV-ozone (UVO) treatment for 30 min. A 2PACz layer (0.3 mg mL^{-1} in ethanol) was spin-coated (3000 rpm, 20 s) on the pre-cleaned ITO/glass substrates, followed by TA treatment at 100°C for 3 min and VIC treatment under 1×10^{-4} bar for 10 min. The active layer was then formed by spin-coating (3000 rpm, 20 s) a chloroform solution containing D18:L8-BO (1:1.4, w/w), where the D18 concentration was fixed at 5 mg mL^{-1}. The resulting film underwent TA treatment (100°C, 5 min) and VIC treatment (1×10^{-4} bar, 10 min), respectively. The PNDIT-F3N electron transport layer (1.4 mg mL^{-1} in methanol with 0.5 v/v% acetic acid) was then spin-coated (4200 rpm, 20 s) onto the active layer. Finally, 100-nm-thick Ag electrodes were thermally evaporated through a shadow mask to complete the device fabrication. Flexible devices featured a Ag alloy/2PACz/active layer/PNDIT-F3N/Ag architecture, with fabrication procedures otherwise identical to those of rigid devices. The active area of the small-area device was 5.12 mm^2 and was measured by the aperture of 3.15 mm^2. For the 1 cm^2 device, the active area was 1.27 cm^2 and was measured by the aperture of 1.0 cm^2.

OSC modules with active areas of 15.7 cm^2 and 67.2 cm^2 were fabricated on 5×5 cm^2 and 10×10 cm^2 ITO glass substrates, respectively. The geometrical design of modules are shown in Supplementary Fig. 27. The aperture areas are 16.80 cm^2 for the small module and 72 cm^2 for the large module. The modules employed an architecture analogous to that of the small-area devices, comprising 8 and 16 series-connected sub-cells. Series interconnections were established via P1,

P2, and P3 patterning lines, with P1 and P3 widths set to 20 μm and 90 μm, respectively. During fabrication, a PEDOT:PSS layer was blade-coated onto the cleaned substrates at 25 mm s^{-1} and annealed at 150°C for 15 min in ambient air. Subsequently, the active layer (5 mg mL^{-1}) was blade-coated (25 mm s^{-1}, 20 μm gap height) and subjected to vacuum treatment at 1×10^{-4} bar for 10 min to achieve a thickness of ~105 nm. A PNDIT-F3N electron transport layer (0.8 mg mL^{-1} in methanol) was then blade-coated on top (25 mm s^{-1}, 8 μm gap height). Finally, 100 nm Ag electrodes were thermally evaporated at 1×10^{-6} mbar to complete the devices.

Optoelectronic properties

Current density-voltage (*J-V*) characteristics were acquired using a computer-controlled Keithley 2450 Source Measure Unit under AM 1.5G illumination (100 mW cm^{-2}), with the light intensity calibrated by an Enlitech standard solar cell. The *J-V* curves of small-area and 1.0 cm^2 area devices were obtained along the forward scan direction from -0.02 V to 1 V, with a scan step of 20 mV and a dwell time of 1 ms. The *J-V* curves characteristics of 15.7 cm^2 area devices were obtained along the forward scan direction from -0.3 V to 7.3 V, with a scan step of 20 mV and a dwell time of 1 ms. *J-V* curves were measured under a temperature of 25 ℃ in a glove box filled with nitrogen. EQE spectra were recorded using an Enlitech QE-R measurement system, with the wavelength range from 300 to 900 nm.

UV–visible absorption

It was carried out with a Cary 60 spectrometer, and all film samples were spin-cast on quartz glass substrates.

SCLC measurements

For SCLC tests, the device structures were specifically designed for each carrier type. Dedicated device architectures were employed: ITO/PEDOT:PSS/active layer/Ag for hole-only devices and ITO/ZnO/active layer/PNDIT-F3N/Ag for electron-only devices. The carrier mobilities were extracted by fitting the *J*-*V* characteristics to the Mott-Gurney law through the following equation:

$$J = \frac{9}{8}\varepsilon_r\varepsilon_0\mu\frac{V^2}{L^3} \quad (3)$$

where J represents the current density, ε_0 denotes the vacuum permittivity, ε_r is the relative permittivity of the material, μ corresponds to the zero-field mobility, V is the applied voltage, and L is the film thickness[43].

Time-resolved femtosecond transient absorption (TA) spectroscopy

The TA spectroscopy measurements were performed on an Ultrafast Helios pump-probe system in collaboration with a regenerative amplified laser system from Coherent[44].

Sensitive external quantum efficiency (sEQE) measurements

The sEQE were conducted using the following setup: A 150 W quartz halogen lamp (LSH-75, Newport) served as the light source, with the output beam directed through a monochromator (CS260-RG-3-MC-A, Newport) to generate a tunable monochromatic light. The monochromatic

light was then modulated at 173 Hz using an optical chopper (3502, Newport) before being focused onto the OSC devices. The resulting photocurrent was amplified by a low-noise current preamplifier (SR570, Stanford Research Systems) to minimize noise interference. Finally, the signal was recorded and processed using a lock-in amplifier (SR830 DSP, Stanford Research Systems) to enhance detection sensitivity[45-46].

AFM, PFQNM and KPFM characterizations

Atomic force microscopy (AFM) data were acquired using NanoScope 10 software on a Bruker Dimension Icon microscope equipped with OTESPA-R4 probes (nominal spring constant = 26 N m^{-1}, resonance frequency ~ 300 kHz), operated in Tapping mode. Images were processed by second-order polynomial flattening (background subtraction) using NanoScope Analysis. PFQNM and AFM imaging were performed using the same microscope equipped with ScanAsyst-Air probes (nominal spring constant = 0.4 N m^{-1}, resonance frequency ~ 70 kHz), operating in PeakForce Tapping mode. KPFM was conducted using SCM-PIT-V2 probes (Bruker; Pt/Ir-coated, nominal spring constant = 3 N m^{-1}, resonance frequency ~75 kHz) in amplitude-modulation KPFM mode.

GIWAXS characterizations

AFM was used to characterize the morphology of the device in the tapping mode. GIWAXS measurements were carried out with a Xeuss 2.0 SAXS/WAXS laboratory beamline using an in-

door Cu X-ray source (8.05 keV) and a Pilatus3R 300K detector. Samples were prepared on Si substrates using identical blend solutions as those used in devices.

SEM characterizations

The SEM instrument used was the Zeiss Gemini 300, equipped with an energy-dispersive X-ray spectroscopy (EDS) detector (Oxford X-Max, energy resolution: 125 eV, Mn-Kα) and an electron backscatter diffraction (EBSD) system (Oxford Symmetry S). Samples were treated with a Tousimis Autosamdri-815 critical point dryer, and platinum was sputtered using a Leica ACE200 ion sputter coater to enhance conductivity. Imaging was performed at specified accelerating voltages, with a point resolution of 0.7 nm @ 15 kV achieved by the instrument.

Contact angle measurements

The contact angle measurements of films are performed using a Biolin Scientific Oy 02130 Espoo, Finland Analyzer. Water and EG are used as probe liquids.

Time-of-flight secondary ion mass spectrometry analysis

This test was conducted on a ToF-SIMS M6 mass spectrometer (ION-TOF GmbH, Munster, Germany). Mass spectra were collected by a 30 keV Bi_3^+ liquid metal cluster ion gun (LMIG) as analysis beam in high current bunched mode. The Bi_3^+ primary ion source was operated using a pulsed beam at 10 kHz and the analyzer was operated in high mass resolution mode. An argon gas cluster ion source (GCIB, 5 kV, 1 nA) was employed as sputter gun. Negative ion spectra were

calibrated by O^-, OH^-, C_2^-, C_2H^-, and Cl^-, etc. Data were processed by ION-TOF SurfaceLab software (Version 7.4, ION-TOF GmbH) by signal of fragment ions. The signals were displayed on a color scale, which were directly related to the intensities of detected ions of interest[47].

3M tape peeling tests

The model of the universal testing machine is CMT6104. For the peeling tests, the samples were first compressed under 20 N for 30 s to ensure uniform contact, then subjected to five 180° peeling cycles at 300 mm min^{-1}.

Nano-scratch test

Prior to testing, all samples were carefully leveled to ensure surface flatness, which is critical for obtaining reliable scratch test results. Scratch tests were then performed under progressively increasing normal loads using a nanoindentation system (Hysitron Inc. of the United States) equipped with a Berkovich pyramidal diamond indenter, allowing comparative evaluation of TA- and VIC-treated samples[48]. The nano-scratch tests were performed under controlled conditions (maximum load: 1500 μN, loading rate: 100 μN s^{-1}, and scratch rate: 1 μm s^{-1}).

Nanoindentation test

The nanoindentation tests were performed using a Hysitron TI 950 manufactured by Hysitron Inc. of the United States, featuring a test sensitivity of less than 30 nN and 0.2 nm. The indenter was a Berkovich pyramidal diamond indenter, with an angle of 65.3° between the centerline and the

surface, a surface angle of 142.3°, and an indenter diameter of 100 nm. The displacement control mode was configured, with a maximum displacement of 50 nm. The loading, unloading and holding times were all 5 s. The hardness (H) and the reduced modulus (E_r) can be computed by the following formulas:

$$H = \frac{P}{A}, E_r = \frac{\sqrt{\pi}S}{2\beta\sqrt{A}} \quad (4)$$

where P represents the real-time load at any indentation depth, and A is the projected area of the contact surface under the action of P. The E_r can be employe to account for the elastic deformation of the indenter and the specimen, and β is a constant related to the shape of the indenter (1.034 for the Berkovich indenter). The S is the slope of the curve at the unloading point.

DATA AVAILABILITY

The data generated in this study are provided in the Source Data file published alongside this paper.

REFERENCES

1. Ma, R. et al. Organic solar cells: beyond 20%. *Sci. China Mater.* **68**, 1689–1701 (2025).
2. Balasubramanian, K. et al. Neural network-based Bluetooth synchronization of multiple wearable devices. *Nat. Commun*. **14**, 4472 (2023).
3. Yang, C., Zhang, S. & Hou, J. Low-cost and efficient organic solar cells based on polythiophene and poly(thiophene vinylene)-related donors. *Aggregate* **3**, e111 (2022).
4. Zou, W. et al. Patterned growth of polyaniline nanowire arrays on a flexible substrate for high-performance gas sensing. *Small* **7**, 3287–3291 (2011).

5. Zhang, D. et al. Achieving highly efficient, mechanically robust and thermally stable organic solar cells through optimizing the branching position and side chain length of small molecule acceptors. *Energy Environ. Sci*. **18**, 2342–2352 (2025).
6. Ye, Q. et al. Ductile oligomeric acceptor-modified flexible organic solar cells show excellent mechanical robustness and near 18% efficiency. *Adv. Mater.* **35**, 2305562 (2023).
7. Chen, L. et al. Exploiting the donor-acceptor-additive interaction's morphological effect on the performance of organic solar cells. *Aggregate* **5**, e455 (2024).
8. Li, C. et al. Highly efficient organic solar cells enabled by suppressing triplet exciton formation and non-radiative recombination. *Nat. Commun*. **15**, 8872 (2024).
9. Gong, R. et al. A strain relaxation modulation for printing high-performance flexible Pseudo-Planar heterojunction organic solar cells. *Adv. Mater.* **37**, 2501033 (2025).
10. Liu, F. et al. Organic solar cells with 18% efficiency enabled by an alloy acceptor: a two-in-one strategy. *Adv. Mater*. **33**, 2100830 (2021).
11. Yuan, J. et al. Single-junction organic solar cell with over 15% efficiency using fused-ring acceptor with electron-deficient core. *Joule* **3**, 1140–1151 (2019).
12. Zeng, G. et al. Realizing 17.5% efficiency flexible organic solar cells via atomic-level chemical welding of silver nanowire electrodes. *J. Am. Chem. Soc*. **144**, 8658–8668 (2022).
13. Xu, Z. et al. Thermoplastic elastomer enhanced interface adhesion and bending durability for flexible organic solar cells. *NPJ Flex. Electron*. **6**, 56 (2022).
14. Wang, J. et al. Intrinsically stretchable organic photovoltaics by redistributing strain to PEDOT:PSS with enhanced stretchability and interfacial adhesion. *Nat. Commun.* **15**, 4902

(2024).

15. Tan, L. et al. Highly efficient flexible polymer solar cells with robust mechanical stability. *Adv. Sci*. **6**, 1801180 (2019).
16. Chong, K. et al. Realizing 19.05% efficiency polymer solar cells by progressively improving charge extraction and suppressing charge recombination. *Adv. Mater*. **34**, 2109516 (2022).
17. Chen, X. et al. Realizing ultrahigh mechanical flexibility and > 15% efficiency of flexible organic solar cells via a "welding" flexible transparent electrode. *Adv. Mater*. **32**, 1908478 (2020).
18. Chen, Y. et al. "Reinforced concrete"-like flexible transparent electrode for organic solar cells with high efficiency and mechanical robustness. *Sci. China Chem*. **65**, 1164–1172 (2022).
19. Fanady, B., Song, W., Peng, R., Wu, T. & Ge, Z. Efficiency enhancement of organic solar cells enabled by interface engineering of sol-gel zinc oxide with an oxadiazole-based material. *Org. Electron*. **76**, 105483 (2020).
20. Li, H. et al. Molecularly Interlocked interfaces enable record-efficiency stretchable organic photovoltaics. *Adv. Mater*. **37**, 2507761 (2025).
21. Yang, K. et al. Molecular lock induced by chloroplatinic acid doping of PEDOT:PSS for high-performance organic photovoltaics. *ACS Appl. Mater. Interfaces* **12**, 30954–30961 (2020).
22. Lee, I., Noh, J., Lee, J. Y. & Kim, T. S. Cooptimization of adhesion and power conversion efficiency of organic solar cells by controlling surface energy of buffer layers. *ACS Appl. Mater. Interfaces* **9**, 37395–37401 (2017).
23. Han, Y. et al. Efficiency above 12% for 1 cm^2 flexible organic solar cells with Ag/Cu grid

transparent conducting electrode. *Adv. Sci*. **6**, 1901490 (2019).

24. Juillard, S. et al. Mechanical reliability of flexible encapsulated organic solar cells: characterization and improvement. *ACS Appl. Mater. Interfaces* **10**, 29805–29813 (2018).
25. Li, S., Li, Z., Wan, X. & Chen, Y. Recent progress in flexible organic solar cells. *eScience* **3**, 100085 (2023).
26. Sun, Y. et al. Flexible organic photovoltaics based on water-processed silver nanowire electrodes. *Nat. Electron*. **2**, 513–520 (2019).
27. Song, W. et al. Ultra robust and highly efficient flexible organic solar cells with over 18% efficiency realized by incorporating a linker dimerized acceptor. *Angew. Chem. Int. Ed*. **62**, e202310034 (2023).
28. He, H. et al. Dynamic hydrogen-bonding enables high-performance and mechanically robust organic solar cells processed with non-halogenated solvent. *Nat. Commun.* **16**, 787 (2025).
29. Gregori, A. et al. The role of donor polymer and PEDOT:PSS formulation on adhesion processes in inverted organic solar cells. *Sol. Energy Mater. Sol. Cells* **174**, 25–33 (2018).
30. Jiang, W. et al. Design of intrinsically stable hole-selective self-assembled monolayers by introducing fused-ring intramolecular donor–acceptor interactions. *Angew. Chem. Int. Ed.* **64**, e202507273 (2025).
31. Dupont, S. R., Voroshazi, E., Heremans, P. & Dauskardt, R. H. Adhesion properties of inverted polymer solarcells: Processing and film structure parameters. *Org. Electron*. **14**, 1262–1270 (2013).
32. Samir, M., Sacramento, A., Almora, O., Pallarès, J. & Marsal, L. F. A facile low prevacuum

treatment to enhance the durability of nonfullerene organic solar cells. *Sol. RRL* **8**, 2400479 (2024).

33. Zhao, W. et al. Vacuum-assisted annealing method for high efficiency printable large-area polymer solar cell modules. *J. Mater. Chem. C* **7**, 3206–3211 (2019).
34. Liu, X. et al. Fluidic manipulating of printable zinc oxide for flexible organic solar cells. *Adv. Mater.* **34**, 2106453 (2022).
35. Wang, Y. et al. A novel upside-down thermal annealing method toward high-quality active layers enables organic solar cells with efficiency approaching 20%. *Adv. Mater.* **36**, 2411957 (2024).
36. Li, Y. Hybrid interfacial engineering enables organic solar cells to 21% efficiency. *Sci. China Mater.* (2025).
37. Li, C. et al. Non-fullerene acceptors with branched side chains and improved molecular packing to exceed 18% efficiency in organic solar cells. *Nat. Energy* **6**, 605–613 (2021).
38. Li, C. et al. Achieving record-efficiency organic solar cells upon tuning the conformation of solid additives. *J. Am. Chem. Soc*. **144**, 14731–14739 (2022).
39. Liu, C. et al. Oligomeric carbazole phosphonic acid as hole-transporting layer for organic solar cells with efficiency of 19.63%. *Adv. Funct. Mater.* **35**, 2417786 (2025).
40. Li, C. et al. Organic solar cells with 21% efficiency enabled by a hybrid interfacial layer with dual-component synergy. *Nat. Mater.* **24**, 1626–1634 (2025).
41. Wu, S. Calculation of interfacial tension in polymer systems. *J. Polym. Sci. Part C Polym. Symp*. **34**, 19–30 (2007).

42. Li, H. et al. Synergistic multimodal energy dissipation enhances certified efficiency of flexible organic photovoltaics beyond 19%. *Adv. Mater*. **37**, 2411989 (2024).

43. Ye, Q. et al. The butterfly-effect of flexible linkers in giant-molecule acceptors: optimized crystallization and aggregation for enhancing mechanical durability and approaching 19% efficiency in binary organic solar cells. *Energy Environ. Sci.* **18**, 4373 (2025).

44. Song, X. et al. Process-Aid Solid Engineering Triggers Delicately Modulation of Y-Series Non-Fullerene Acceptor for Efficient Organic Solar Cells. *Adv. Mater.* 34, 2200907 (2022).

45. Qian, D. et al. Design rules for minimizing voltage losses in high-efficiency organic solar cells. *Nat. Mater.* **17**, 703-709 (2018).

46. Yao, J. et al. Quantifying Losses in Open-Circuit Voltage in Solution-Processable Solar Cells. *Phys. Rev. Appl.* **4**, 014020 (2015).

47. Zhan, Y. et al. Nacre inspired robust self-encapsulating flexible perovskite photodetector. Nano Energy **98**, 107254 (2022).

48. Hang, Y. et al. Mechanical properties and interfacial adhesion of composite membranes probed by in-situ nano-indentation/scratch technique. *Membr. Sci.* **494**, 205 (2015).

ACKNOWLEDGEMENTS

The authors acknowledge the financial support from the NSFC (52450063 to H.H., 52120105006 to H.H., 52522314 to Y.C. and 52473200 to Y.C.), the Fundamental Research Funds for the Central Universities (E4ER1801 to H.H. and E3ET1803 to H.H.), and the Strategic Priority Research Program of Chinese Academy of Sciences (XDB 0520103 to H.H.).

AUTHOR CONTRIBUTIONS

H.H., Y.C. and S.W. developed the concept and conceived the idea. H.H., Y.C. supervised and directed this project. S.W., R.D. and J.W. participated in the optimization of device fabrication. S.W. and Z.Z. prepared samples for characterization analysis. S.W., R.D. and Z.Z. analyzed and processed data. S.W. and R.D. wrote the manuscript and H.H., Y.C. contributed to revisions of the manuscript. Z.X. and Y.L. conducted the TA measurements and data analysis. Z.T. and J.W. conducted the energy loss measurements and data analysis. J.Z. carried out the GIWAXS measurements. Y.Z. contributed to the TOF-SIMS measurements. All the authors participated in the data analysis and commented on the manuscript.

COMPETING INTERESTS

The authors declare no competing interests.

Editorial summary:

Organic solar cells face morphological and interfacial limits that reduce efficiency and stability. The authors present a vacuum-induced compaction method that builds dense, smooth interfaces, delivering large area-scalable high-performance devices.

Peer review information: *Nature Communications* thanks Hae Jung Son, and the other, anonymous, reviewer(s) for their contribution to the peer review of this work. A peer review file is available.